Minimal model of drag in one-dimensional crystals

Harshitra Mahalingam,[1] Zhun Wai Yap,[2] B. A. Olsen,[2,3,*] and A. Rodin[2,4,5,†]

[1]*Institute for Functional Intelligent Materials, National University of Singapore, 4 Science Drive 2, 117544, Singapore*
[2]*Yale-NUS College, 16 College Avenue West, 138527, Singapore*
[3]*Department of Physics, National University of Singapore, 2 Science Drive 3, 117551 Singapore*
[4]*Centre for Advanced 2D Materials, National University of Singapore, 117546, Singapore*
[5]*Materials Science and Engineering, National University of Singapore, 117575, Singapore*

(Received 13 September 2022; revised 21 December 2022; accepted 12 January 2023; published 27 January 2023)

Using a nonperturbative classical approach, we study the dynamics of a mobile particle interacting with an infinite one-dimensional (1D) chain of harmonic oscillators. This minimal system is an effective model for many 1D transport phenomena, such as molecular motion in nanotubes and ionic conduction through solid-state materials. As expected, coupling between the mobile particle and the chain induces dissipation of the mobile particle's energy. However, both numerical and analytic results demonstrate an unconventional nonmonotonic dependence of the drag on particle speed. In addition, when this system is subjected to a constant bias, it supports multiple steady-state drift velocities.

DOI: 10.1103/PhysRevResearch.5.013053

I. INTRODUCTION

In general, transport through a medium is accompanied by energy loss [1], leading to many familiar phenomena such as aerodynamic drag and friction. Most classical formulations of dissipation, with the notable exception of friction, focus on liquid or gaseous media [1,2]. In these models, the size and energy scales of the moving object often significantly exceed those of the microscopic degrees of freedom (atoms and molecules of the medium). This scale difference allows a series of simplifications, such as treating the medium as a continuous substance and regarding the drag force as local in time [3–5]. However, if the size of the mover is smaller than or comparable to the interatomic spacing of the medium, as in many solids, we cannot treat the medium as a continuous fluid. Many of these solid systems also exhibit significant correlations, which can make the drag nonlocal in both time and space. If the mover is an ion, the size and energy scales of the mover and the solid's ions become comparable, requiring that their dynamics are treated on equal footing, complicating the problem substantially.

A relevant example of such a scenario is ionic transport through solids, which has been garnering attention recently in the context of solid-state batteries [6–8], as a part of the search for more sustainable energy storage technologies [9,10]. An important component of these batteries is the solid electrolyte: an electronic insulator that can conduct ions and acts as a separator between the anode and the cathode. The most commonly used tools for studying ionic motion in ionic conductors are classical molecular dynamics (MD) and *ab initio* molecular dynamics simulations [11–21]. These studies are particularly useful for elucidating which lattice structures produce lower energy barriers for the mobile ions and how the lattice dynamics impact the ionic transport. These techniques are, however, less suitable for studying dissipation in the long-time limit as the simulations are typically restricted to time periods on the order of nanoseconds. Therefore, an analytical approach that makes it possible to explore the emergence of dissipation in solid materials while treating the motion of the solid's ions and the current carriers on equal footing is desired.

Earlier work [22] related the mobile ion's energy dissipation to the potential profile through which it moves. The study assumed that the interaction between the mobile ion and the solid could be viewed as local in time to make the problem tractable. Here, we relax this assumption by focusing on the simplest crystal, a 1D atomic chain, shown in Fig. 1.

We start by demonstrating the emergence of drag in a 1D crystal using numerical calculations and compare the results to the predictions of an analytical model in the absence of thermal motion. We show that the interplay of geometry and the structure of the crystal lead to an unconventional dependence of drag on speed, where the energy loss is nonmonotonic in the velocity, decreasing with higher speeds. Furthermore, we predict that applying a bias to the system gives rise to multiple drift velocities, the values of which are determined by the crystal parameters. Numerical confirmation of this prediction lends credence to our model as an appropriate tool for the problem, paving the way for subsequent studies focusing on higher dimensions and the role of thermal effects on transport.

The 1D crystal model is easy to study both analytically and numerically, providing a valuable platform for

*Corresponding author: ben.olsen@yale-nus.edu.sg
†Corresponding author: aleksandr.rodin@yale-nus.edu.sg

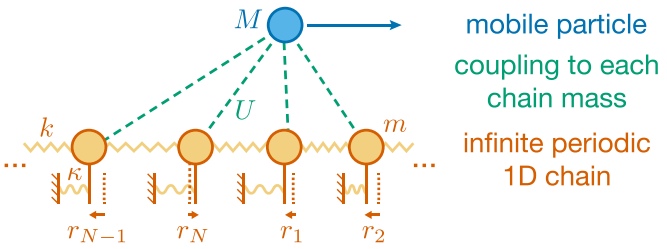

FIG. 1. *Schematic of the system.* A mobile particle of mass M moves along a periodic 1D chain of $N \to \infty$ identical masses m, separated by distance a at equilibrium. Each chain mass is confined by a harmonic potential with force constant κ, in addition to coupling to its neighbors harmonically with force constant k. The displacement of each mass from its equilibrium position is r_g. The N oscillatory modes of the chain act as a bath, absorbing the mobile particle's energy due to the interaction U.

developing an intuitive understanding of the dissipative motion in crystals. Being classical, the system is tractable even when the interaction between the mover and the framework is nonlinear, unlike some well-established quantum models, such as Caldeira-Leggett [23] and Hu-Paz-Zhang [24], as well as more recent works [25,26] that rely on a linear coupling for integrating out the medium degrees of freedom.

Our model could be adapted to describe a range of experimentally relevant systems. In some highly anisotropic ionic conductors, current-carrying ions travel along 1D channels [27–30] or nanowires [31], similar to motion in nanotubes of atoms [32–35], simple molecules [36,37], or fullerenes [38,39].

In Sec. II, we derive the equations of motion for a collection of mobile particles traveling through a potential landscape generated by a vibrating lattice of an arbitrary dimensionality. We then simplify the expressions to focus on the relevant one-dimensional system in Sec. III. In Sec. IV, we demonstrate the dissipative motion of a particle along the chain and derive an analytic expression for the particle's energy loss. We validate the analytic expression in the single collision (Sec. V) and long-time (Sec. VI) limits. Conclusions can be found in Sec. VII.

We perform all our calculations using the JULIA programming language [41] and make our code available at Ref. [40]. Due to their size, the output files are not included in the repository. The computational procedure and the justification for our parameter choice are outlined in Appendix. Our plots are visualized using Makie.jl, [42] employing a color scheme suitable for color-blind readers, developed in Ref. [43].

II. GENERAL MODEL

The general model used to describe the motion of mobile particles through a framework (or lattice) of masses with vibrational modes is the same as the one used in Refs. [22,44]. The starting point is the Lagrangian

$$L = T_M(\dot{\mathbf{R}}) - V_M(\mathbf{R}) + T_F(\dot{\mathbf{r}}) - V_F(\mathbf{r}) - U(\mathbf{r}, \mathbf{R}, t), \quad (1)$$

where $\mathbf{r} = \bigoplus_{j=1} \mathbf{r}_j$ and $\mathbf{R} = \bigoplus_{j=1} \mathbf{R}_j$ are vectors whose elements are the displacements of all the framework masses from their equilibrium positions and the positions of the mobile particles, respectively. $T_M(\dot{\mathbf{R}})$ and $T_F(\dot{\mathbf{r}})$ are the kinetic energies of the mobile particles and framework masses, and $V_M(\mathbf{R})$ and $V_F(\mathbf{r})$ are the time-independent potential energies for the two groups of objects. Finally, $U(\mathbf{r}, \mathbf{R}, t)$ is a general potential energy that describes the interaction between the framework and mobile particles, as well as any time-dependent perturbations.

For the mobile particles, the equations of motion take a straightforward form

$$\overleftrightarrow{M}\ddot{\mathbf{R}} = -\nabla_{\mathbf{R}}[U(\mathbf{r}, \mathbf{R}, t) + V_M(\mathbf{R})]. \quad (2)$$

Here, $\overleftrightarrow{M} = \bigoplus_{j=1} M_j \overleftrightarrow{1}_D$ is a block-diagonal matrix where M_j is the mass of the jth mobile particle and D is the system dimensionality.

The treatment of the framework is somewhat more involved given its infinite size. We begin by neglecting interactions with the mobile particle to find a homogeneous solution. Rewriting the framework Lagrangian using the harmonic approximation yields

$$T_F(\dot{\mathbf{r}}) - V_F(\mathbf{r}) \to \tfrac{1}{2}\dot{\mathbf{r}}^T \overleftrightarrow{m}\dot{\mathbf{r}} - \tfrac{1}{2}\mathbf{r}^T \overleftrightarrow{V}\mathbf{r}, \quad (3)$$

with $\overleftrightarrow{m} = \bigoplus_{j=1} m_j \overleftrightarrow{1}_D$, where m_j is the mass of the jth framework mass and $\overleftrightarrow{V}$ is the harmonic coupling matrix. Equation (3) produces the homogeneous equation of motion $\overleftrightarrow{m}\ddot{\mathbf{r}} = -\overleftrightarrow{V}\mathbf{r}$, which can be transformed into a symmetric eigenvalue problem by first defining $\tilde{\mathbf{r}} = \overleftrightarrow{m}^{\frac{1}{2}}\mathbf{r}$ so

$$\ddot{\tilde{\mathbf{r}}} = -\Omega_j^2 \tilde{\mathbf{r}} = -\overleftrightarrow{m}^{-\frac{1}{2}} \overleftrightarrow{V} \overleftrightarrow{m}^{-\frac{1}{2}} \tilde{\mathbf{r}} \equiv -\overleftrightarrow{\tilde{V}}\tilde{\mathbf{r}}, \quad (4)$$

with normalized eigenvectors $\boldsymbol{\varepsilon}_j$ and corresponding eigenvalues Ω_j^2. Consequently, we have $\tilde{\mathbf{r}}(t) = \overleftrightarrow{\varepsilon}\boldsymbol{\zeta}(t)$, leading to $\mathbf{r}(t) = \overleftrightarrow{m}^{-\frac{1}{2}}\overleftrightarrow{\varepsilon}\boldsymbol{\zeta}(t)$, where $\boldsymbol{\zeta}(t)$ is a column vector of normal coordinates giving the amplitude of each mode and $\overleftrightarrow{\varepsilon} = [\boldsymbol{\varepsilon}_1, \boldsymbol{\varepsilon}_2, \dots]$ is a row of column vectors $\boldsymbol{\varepsilon}_j$.

Equipped with a basis of homogeneous solutions, we now include $U(\mathbf{r}, \mathbf{R}, t)$ in the framework equation of motion to give the full equation of motion

$$\begin{aligned} \overleftrightarrow{m}\ddot{\mathbf{r}} &= -\overleftrightarrow{V}\mathbf{r} - \nabla_{\mathbf{r}} U(\mathbf{r}, \mathbf{R}, t) \\ \to \ddot{\boldsymbol{\zeta}} &= -\overleftrightarrow{\Omega}^2\boldsymbol{\zeta} - \overleftrightarrow{\varepsilon}^{-1}\overleftrightarrow{m}^{-\frac{1}{2}}\nabla_{\mathbf{r}} U(\mathbf{r}, \mathbf{R}, t), \end{aligned} \quad (5)$$

where $\overleftrightarrow{\Omega}^2 = \overleftrightarrow{\varepsilon}^{-1}\overleftrightarrow{\tilde{V}}\overleftrightarrow{\varepsilon}$ is a diagonal matrix of the squared eigenfrequencies. For a single normal coordinate, the equation of motion takes the form of a forced harmonic oscillator $\ddot{\zeta}_j = -\Omega_j^2\zeta_j - f_j$. Using the Green's function for a harmonic oscillator

$$G_j(t, t') = \frac{\sin[\Omega_j(t - t')]}{\Omega_j}\Theta(t - t'), \quad (6)$$

we obtain the solution to the driven oscillator problem

$$\begin{aligned} \zeta_j(t) = \zeta_j^H(t) - \int^t dt' \frac{\sin[\Omega_j(t - t')]}{\Omega_j} \\ \times [\overleftrightarrow{\varepsilon}^{-1}\overleftrightarrow{m}^{-\frac{1}{2}}\nabla_{\mathbf{r}} U(\mathbf{r}, \mathbf{R}, t')]_j, \end{aligned} \quad (7)$$

where $\zeta_j^H(t)$ is the homogeneous solution. The subscript j at the brackets indicates that we pick out the jth element of the column vector. Because $\overleftrightarrow{\varepsilon}$ is a row of normal-mode eigenvectors, it is an orthogonal matrix if the eigenvectors

are real and a unitary matrix if the eigenvectors are complex. Taking the more general case of complex eigenvectors, we replace $\overleftrightarrow{\varepsilon}^{-1} \to \overleftrightarrow{\varepsilon}^{\dagger}$ and get

$$\zeta_j(t) = \zeta_j^H(t) - \int^t dt' \frac{\sin[\Omega_j(t-t')]}{\Omega_j} \boldsymbol{\varepsilon}_j^{\dagger} \overleftrightarrow{m}^{-\frac{1}{2}} \nabla_{\mathbf{r}} U(\mathbf{r}, \mathbf{R}, t'). \tag{8}$$

Finally, using $\mathbf{r}(t) = \overleftrightarrow{m}^{-\frac{1}{2}} \sum_j \boldsymbol{\varepsilon}_j \zeta_j(t)$, we obtain

$$\mathbf{r}(t) = \overleftrightarrow{m}^{-\frac{1}{2}} \sum_j \boldsymbol{\varepsilon}_j \zeta_j^H(t) - \int^t dt' \overleftrightarrow{m}^{-\frac{1}{2}} \overleftrightarrow{G}(t-t') \overleftrightarrow{m}^{-\frac{1}{2}} \nabla_{\mathbf{r}} U(\mathbf{r}, \mathbf{R}, t'), \tag{9}$$

$$\overleftrightarrow{G}(t) = \sum_j \boldsymbol{\varepsilon}_j \boldsymbol{\varepsilon}_j^{\dagger} \frac{\sin(\Omega_j t)}{\Omega_j}. \tag{10}$$

Equation (9) gives $\mathbf{r}(t)$ as a combination of a homogeneous trajectory and a memory term originating from the framework's interaction with the mobile particles. This term depends on the entire past history of the system, and the memory kernel G is given by Eq. (10).

Formally, for an infinitely large system, $\mathbf{r}(t)$ contains an infinite number of components. However, because we are primarily interested in the motion of the mobile particles, we only need to keep track of the components of $\mathbf{r}(t)$ which enter Eq. (2). Our memory formulation allows us to compute only a subset of the framework coordinates while retaining an infinite number of degrees of freedom. This focus makes the problem manageable, while retaining the framework's ability to act as a thermal bath and eliminating any periodic effects that could arise in a finite-size system.

The homogeneous solution for a single normal mode ζ_j, described by the Lagrangian $L_j = \dot{\zeta}_j^2/2 - \Omega^2 \zeta_j^2/2$, is $\zeta_j^H(t) = A_j e^{-i\Omega_j t - i\phi_j}$. Here the phase $0 \leqslant \phi_j < 2\pi$ is determined by boundary conditions and the amplitude of the mode A_j is determined by the thermodynamic properties of the framework. To generate the $\mathbf{r}(t)$ originating from the thermal motion, we obtain a set of ϕ_j and A_j that correctly reflects the system's thermodynamics. The phases ϕ_j are sampled from a uniform distribution $[0, 2\pi)$. For A_j, we recall that the amplitude is related to the total energy of the oscillator mode. By treating the possible energies of each mode as a discrete spectrum, following the solution of the quantum mechanical harmonic oscillator, we set the amplitude to a function of the number of quanta n: $A_j(n)$. Using the familiar result for a quantum harmonic oscillator $\langle \mathrm{Re}[\zeta_j(t)]^2 \rangle = \frac{\hbar}{\Omega_j}[n_B(\Omega_j) + \frac{1}{2}]$, we find that $A_j(n_j) = \sqrt{n_j + \frac{1}{2}}\sqrt{\frac{2\hbar}{\Omega_j}}$, where n_j is an integer obtained from the probability distribution $e^{-n\Omega_j/\Omega_T}$.

III. 1D CHAIN

Restricting our attention to 1D crystals, the role of the framework will be played by an infinitely long periodic chain of $N \to \infty$ identical masses m separated by distance a and connected by identical springs with force constant k. In addition to being restricted to one-dimensional motion along the length of the chain, each chain mass is confined by an external harmonic potential with force constant κ to suppress zero-frequency modes which can cause issues in low-dimensional systems. For such a system, the vibrational eigenmodes have frequencies

$$\Omega_j = \sqrt{\Omega_{\mathrm{slow}}^2 + \left(\Omega_{\mathrm{fast}}^2 - \Omega_{\mathrm{slow}}^2\right) \sin^2\left(\frac{q_j a}{2}\right)}, \tag{11}$$

with corresponding normalized eigenvectors $\varepsilon_{g,j} = e^{iq_j a g}/\sqrt{N}$ for $q_j = 2\pi j/aN$ with $1 \leqslant j \leqslant N$, where $1 \leqslant g \leqslant N$ is the index of the chain mass. Here, $\Omega_{\mathrm{fast}} = \sqrt{4k/m + \kappa/m}$ and $\Omega_{\mathrm{slow}} = \sqrt{\kappa/m}$ are the maximum and minimum frequencies of the eigenmodes.

The structure of the system provides natural time and length scales. We express all frequencies in terms of Ω_{slow}, times in terms of $t_{\mathrm{slow}} = 2\pi/\Omega_{\mathrm{slow}}$, lengths in terms of the quantum oscillator length $l_{\mathrm{slow}} = \sqrt{\hbar/m\Omega_{\mathrm{slow}}}$, and energies in terms of $E_{\mathrm{slow}} = \hbar\Omega_{\mathrm{slow}}$. We also assume that all mobile particles have the same mass M, expressed in terms of m as $\mu = M/m$. We assume that the interaction terms do not carry an explicit time dependence and are restricted to pairwise couplings between the chain masses and the mobile particles $U(\mathbf{r}, \mathbf{R}, t) = \sum_{jk} U(r_k, R_j)$. Then, rewriting Eqs. (2) and (9) in terms of the characteristic quantities yields

$$\boldsymbol{\rho}(\tau) = \sum_j \boldsymbol{\varepsilon}_j \sqrt{n_j + \frac{1}{2}} \sqrt{\frac{2}{\omega_j}} e^{-2\pi i \omega_j \tau + i\phi_j} - 2\pi \int^{\tau} d\tau' \overleftrightarrow{\Gamma}(\tau - \tau') \nabla_{\boldsymbol{\rho}} \Phi[\boldsymbol{\rho}(\tau'), \boldsymbol{\sigma}(\tau')], \tag{12}$$

$$\overleftrightarrow{\Gamma}(\tau) = \sum_j \boldsymbol{\varepsilon}_j \boldsymbol{\varepsilon}_j^{\dagger} \frac{\sin(2\pi\omega_j\tau)}{\omega_j}, \tag{13}$$

$$\ddot{\sigma}_j(\tau) = -(2\pi)^2 \frac{1}{\mu} \sum_k \frac{d}{d\sigma_j} \Phi[\rho_k(\tau), \sigma_j(\tau)], \tag{14}$$

where we used the thermodynamic form of the homogeneous component. Here, $\boldsymbol{\rho} = \mathbf{r}/l_{\mathrm{slow}}$, $\sigma_j = R_j/l_{\mathrm{slow}}$, $\tau = t/l_{\mathrm{slow}}$, $\omega_j = \Omega_j/\Omega_{\mathrm{slow}}$, $\Phi = U/E_{\mathrm{slow}}$, and $\overleftrightarrow{\Gamma} = \overleftrightarrow{G} \cdot \Omega_{\mathrm{slow}}$ The memory kernel $\overleftrightarrow{\Gamma}(\tau)$ is a Toeplitz matrix whose nth diagonal is given by

$$\Gamma_n(\tau) = \frac{2}{\pi} \int_0^{\frac{\pi}{2}} d\theta \cos(2n\theta) \times \frac{\sin\left(2\pi\tau\sqrt{1 + \left(\omega_{\mathrm{fast}}^2 - 1\right)\sin^2\theta}\right)}{\sqrt{1 + \left(\omega_{\mathrm{fast}}^2 - 1\right)\sin^2\theta}}. \tag{15}$$

Physically, Eq. (15) acts as a propagator: following an impulse to the lth chain mass at time τ_0, it describes the displacement of the $(l+n)$th chain mass at time $\tau_0 + \tau$.

Because $\overleftrightarrow{\Gamma}(t)$ describes the propagation of perturbations along the chain, we explore the rate of this propagation by considering the group velocity $d\Omega/dq$. For the dispersion given by Eq. (11), the group velocity is not constant. Taking the second derivative of the dispersion, we find that that the group velocity is maximum for $\sin^2(qa/2) = \Omega_{\mathrm{slow}}/(\Omega_{\mathrm{slow}} + \Omega_{\mathrm{fast}})$ and is equal to $(\Omega_{\mathrm{fast}} - \Omega_{\mathrm{slow}})a/2$, or $\pi\alpha(\omega_{\mathrm{fast}} - 1)$ in terms of dimensionless quantities with $\alpha = a/l_{\mathrm{slow}}$. In the absence of the confinement $\kappa \to 0$ ($\Omega_{\mathrm{slow}} \to 0$), the fastest modes are the long-wavelength sound waves, as expected.

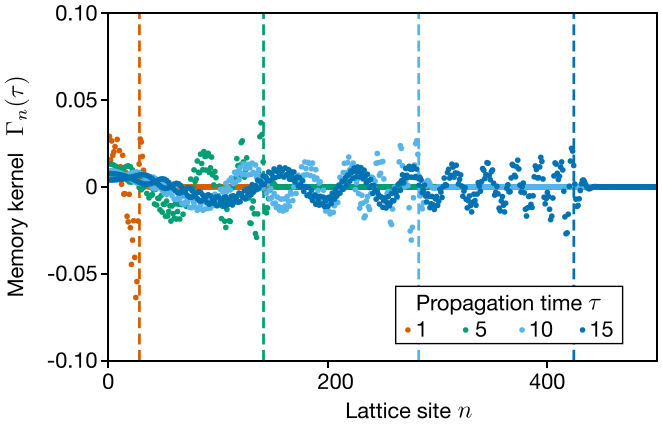

FIG. 2. *Impulse propagation.* Response of chain atoms to an impulse at $\tau = 0, n = 0$ for several $\tau > 0$, shown in different colors. The points indicate the memory kernel $\Gamma_n(\tau)$ for a system with $\omega_{\text{fast}} = 10$. The vertical lines at $n = \tau\pi(\omega_{\text{fast}} - 1)$ coincide with the leading edge of the response, indicating that the disturbance in the chain propagates with the speed of the mode with the highest group velocity.

To illustrate the propagation of impulses, we plot $\Gamma_n(\tau)$ as a function of n for several values of τ in Fig. 2. For each τ, a vertical line at $n = \tau\pi(\omega_{\text{fast}} - 1)$ coincides with the leading edge of the pulse in $\Gamma_n(\tau)$, indicating that the pulse propagates at the fastest group velocity of the phonon band.

IV. DISSIPATION

To discuss some general behaviors of this model, we compute the motion for a system with $\omega_{\text{fast}} = 10$, interaction Φ with Gaussian shape of amplitude $\Phi_0 = \pm 20$ and width $\lambda = 4$, and lattice spacing $\alpha = 40$. We have shown before [44] that $\Omega_{\text{fast}}/\Omega_{\text{slow}} = 10$ provides a sufficiently wide band while keeping the computational time reasonable; see Appendix for more details about the parameter choice and the computational procedure. We introduce a mobile particle with mass $\mu = 1$ and initial velocity $\dot{\sigma}_0 = 120$ midway between two chain masses. As shown in Fig. 3, the mobile particle's kinetic energy decreases, slowing until it eventually becomes trapped in a local energy well. At this scale, it is hard to see, but the mobile particle's velocity undergoes fluctuations as it passes each chain mass.

We also show the displacement $\delta\rho_j$ of the chain masses near the mobile particle using a heat map. The amplitude of these displacements is very small compared to the chain mass spacing ($\delta\rho_j \ll \alpha$) and grows as the mobile particle slows down. Outside a sound cone, the chain masses show no displacement. This cone is well predicted by the greatest group velocity in the phonon band, as discussed above. After the mobile particle becomes trapped, the system undergoes persistent oscillation at frequencies just outside the phonon band, as discussed in Ref. [44].

A. Velocity fluctuation

To explore the velocity variation in detail, we consider the case of a particle passing a single chain mass, where the particle is initialized halfway between two chain masses with

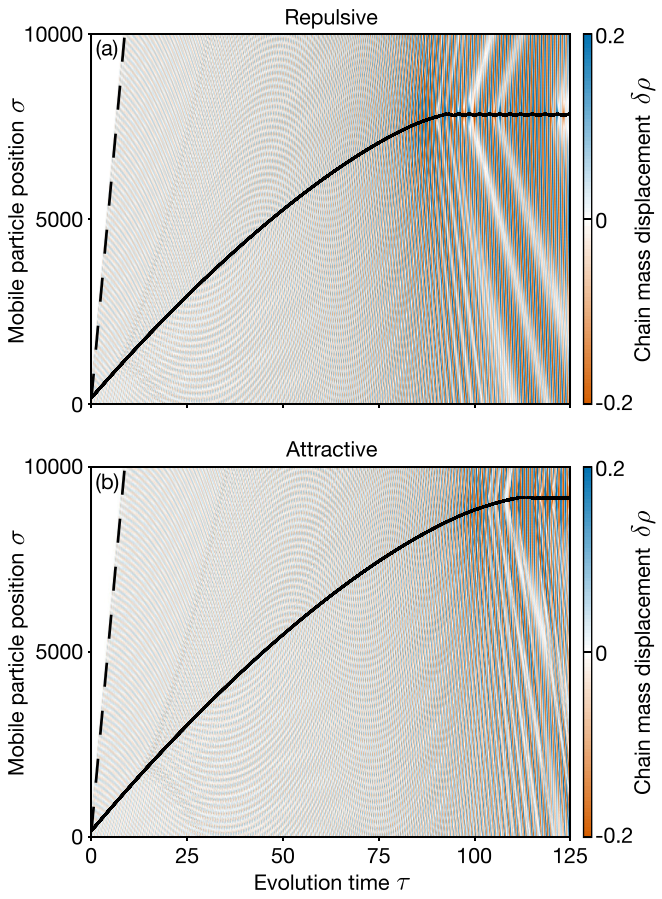

FIG. 3. *General example of dissipation.* Motion of a single mobile particle with repulsive (a) and attractive (b) Gaussian chain-particle interaction. Both cases have chain spacing $\alpha = 40$, Gaussian width $\lambda = 4$, and amplitude $\Phi_0 = \pm 20$, $\mu = 1$, and initial mobile particle speed $\dot{\sigma}_0 = 120$ at a point halfway between chain masses. Both mobile particle trajectories $\sigma(\tau)$, shown in black lines, exhibit gradual slowing and eventual trapping in local energy minima. The displacement of 250 individual chain masses $\delta\rho_j$ is shown with a heat map. At late times, $|\delta\rho_j|$ reaches values as large as 0.8, so the colors are saturated. The dashed lines with slope $\pi\alpha(\omega_{\text{fast}} - 1)$ represent the edge of the sound cone, outside of which the chain masses are motionless.

speed $\dot{\sigma}_0 = 50$. Figures 4(a) and 4(b) show the particle trajectory and velocity for a single chain pass, respectively. The black horizontal dotted line in (a) indicates the rest position of the subsequent chain mass in the particle trajectory. The vertical dotted lines indicate the time at which the particle passes the chain rest mass position, with the colors corresponding to the sign of the potential. We see that the particle in the repulsive system reaches $\sigma = 240$ at a later time than the particle in the attractive system, indicating a difference in velocity between the two cases.

Plotting the particle velocity [Fig. 4(b)] reveals the effect of the interaction potential on the particle and shows that the particle velocity is not constant throughout a single pass. The interaction potential profile Φ determines the velocity profile experienced by the particle. In the repulsive (attractive) case, the particle slows down (speeds up) in the vicinity of the

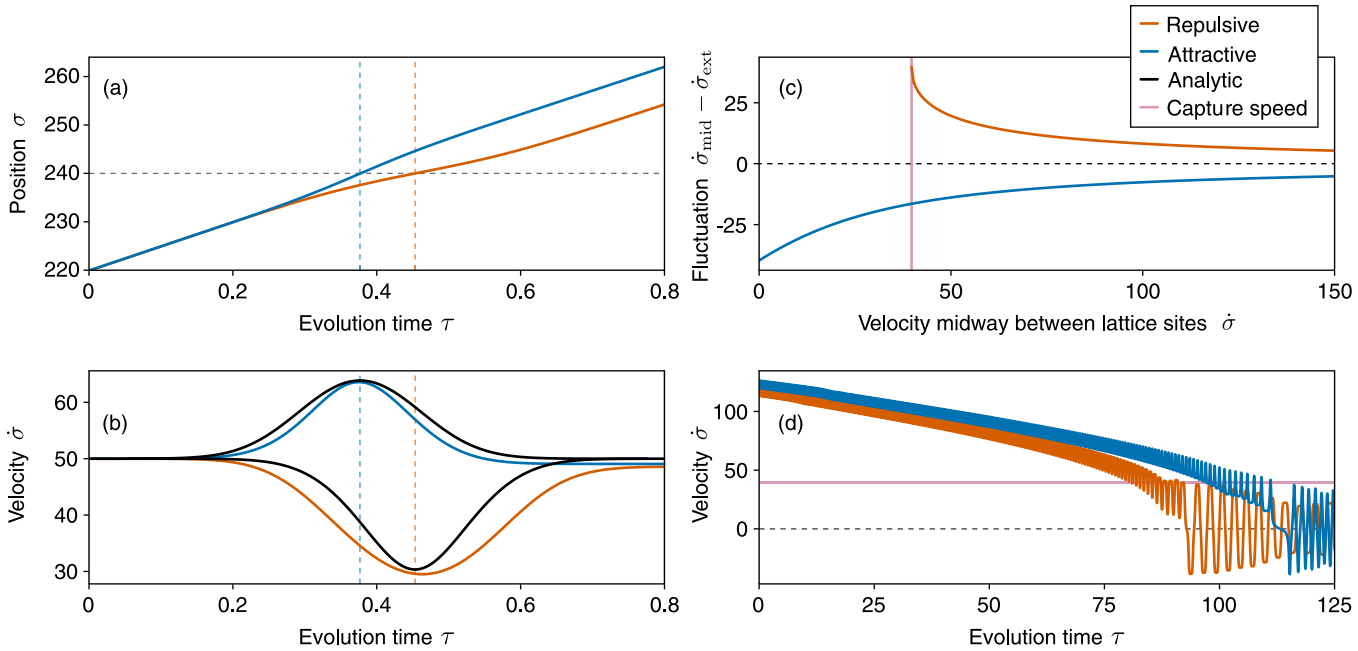

FIG. 4. *Velocity fluctuation close to chain mass.* (a) Particle position σ and (b) velocity $\dot{\sigma}$ for a single chain pass. The system has $\omega_{\text{fast}} = 10$ and a Gaussian interaction profile with $\Phi_0 = \pm 20$ and $\lambda = 4$. The mobile particle is initialized with speed $\dot{\sigma} = 50$ halfway between two chain masses at $\sigma = 220$. The horizontal dotted line in (a) indicates the rest position of the subsequent chain mass, while the vertical dotted lines in both (a) and (b) indicate the time at which the particle passes the chain mass rest position. The black solid lines give the analytic velocity fluctuation for both signs of Φ_0, offset to match the time the particle passes the chain mass rest position. (c) Maximum velocity fluctuations as a function of velocity for $\Phi_0 = \pm 20$. (d) Particle velocity evolution for the trajectories plotted in Fig. 3. The capture speed is given by the pink horizontal line.

chain mass. The vertical dotted lines in Fig. 4(b) are the same as in Fig. 4(a) and correspond to the time at which the particle passes the chain mass *rest position*. The fact that the extrema in the velocity profiles correspond well to these times further validates the claim that the chain mass deviation is small.

We can obtain an approximate analytic form of the velocity fluctuation for the case of a Gaussian potential profile $\Phi(x) = \Phi_0 \exp(-\frac{x^2}{2\lambda^2})$ using a straightforward energy conservation argument. In the case of a conservative process with no energy loss and fixed chain masses, the velocity profile, to leading order, is given by

$$\dot{\sigma}(\tau) = \sqrt{\dot{\sigma}_0^2 - \frac{8\pi^2\Phi_0}{\mu} \exp\left(-\frac{\dot{\sigma}_0^2\tau^2}{2\lambda^2}\right)}, \tag{16}$$

where $\tau \in [-\frac{\alpha}{2\dot{\sigma}_0}, \frac{\alpha}{2\dot{\sigma}_0}]$. We plot this in Fig. 4(b) and see that the analytic expression agrees well with the velocity profile of a particle passing a single chain mass. At the extremum of the interaction profile, the velocity is given by $\dot{\sigma}_{\text{ext}} = \sqrt{\dot{\sigma}_0^2 - 8\pi^2\Phi_0/\mu}$. Figure 4(c) plots the maximum velocity fluctuations $\dot{\sigma}_0 - \dot{\sigma}_{\text{ext}}$ for both signs of Φ_0. The magnitude of the fluctuations increases with lower speed and, in the case of the repulsive potential, there is a minimum speed $\dot{\sigma}_{\text{min}} = \sqrt{8\pi^2\Phi_0/\mu}$ which is required for the particle to overcome the potential barrier. Put another way, the particle in the repulsive case is trapped when its kinetic energy midway between lattice sites falls below Φ_0. In the attractive case, the particle is captured when its kinetic energy *near the chain mass* falls below Φ_0.

The increase in the magnitude of fluctuation is also reflected in Fig. 4(d), which plots the particle velocity over time for the trajectories in Fig. 3. We see the velocity fluctuations as spikes pointing down (up) for the repulsive (attractive) case. The fluctuation magnitudes become larger as the speed decreases. In both cases, the particle eventually becomes trapped by chain masses, as shown by the negative velocities. It is useful to neglect the interaction-induced fluctuation and consider only the particle velocity midway between chain masses, which is given by local maxima (minima) for the repulsive (attractive) case. While the value of the extremum velocity is well-approximated using this method across all velocities, the agreement between analytics and numerics for the full profile becomes worse at lower speeds, where the fluctuation magnitude becomes a significant fraction of the initial velocity.

B. Dissipation scaling

Numerical integration of the equations of motion Eqs. (12)–(14) demonstrates dissipation, as expected. To quantify this dissipative energy loss, we will take advantage of the chain masses' small deflection during their interaction with the particle. Neglecting this deflection turns Eq. (14) into a dissipationless equation of motion:

$$\ddot{\sigma}(\tau) = -(2\pi)^2 \frac{1}{\mu} \frac{d}{d\sigma} \Phi[\boldsymbol{\rho}_0, \sigma(\tau)]. \tag{17}$$

Next, let $\tau = -\tau_*$ be the time when the mobile particle is introduced to the system midway between two chain masses

and $\tau = \tau_*$ be the time when it reaches another, not necessarily the next, midpoint. Assuming that the interaction of the mobile particle with individual chain masses is symmetric, the lack of dissipation in Eq. (17) means that $\dot{\sigma}(\tau) = \dot{\sigma}(-\tau)$ for $-\tau_* \leqslant \tau \leqslant \tau_*$. Rewriting Eq. (7) without the homogeneous part in terms of the dimensionless variables and dropping the displacement of the chain masses yields

$$\begin{aligned}\zeta_j(\tau_*) =& -2\pi\sqrt{\frac{\hbar}{\Omega_{\text{slow}}}} \\ &\times \int_{-\tau_*}^{\tau_*} d\tau \frac{\sin[2\pi\omega_j(\tau_* - \tau)]}{\omega_j} \boldsymbol{\varepsilon}_j^\dagger \nabla_{\boldsymbol{\rho}_0} \Phi[\boldsymbol{\rho}_0, \sigma(\tau)] \\ =& -2\pi\cos(2\pi\omega_j\tau_*)\sqrt{\frac{\hbar}{\Omega_{\text{slow}}}} \\ &\times \int_{-\tau_*}^{\tau_*} d\tau \frac{e^{-2\pi i\omega_j\tau}}{i\omega_j} \boldsymbol{\varepsilon}_j^\dagger \nabla_{\boldsymbol{\rho}_0} \Phi[\boldsymbol{\rho}_0, \sigma(\tau)], \end{aligned} \tag{18}$$

where we used the fact that $\boldsymbol{\varepsilon}_j^\dagger \nabla_{\boldsymbol{\rho}_0} \Phi[\boldsymbol{\rho}_0, \sigma(\tau)]$ is odd in τ, as a consequence of Eq. (17). Setting $\Phi(\boldsymbol{\rho}_0, \sigma) = \sum_n \Phi(\sigma - \alpha n)$ as a sum of individual pairwise interactions and defining the Fourier transform $\Phi_p = \int dx\, e^{ipx}\Phi(x)$, where $p = 2\pi l/(N\alpha)$ for $l \in \mathbb{Z}$, gives

$$\Phi(\boldsymbol{\rho}_0, \sigma) = \frac{1}{N\alpha} \sum_{n,q,Q} e^{-i(q+Q)(\sigma - \alpha n)} \Phi_{q+Q}, \tag{19}$$

where $q = 2\pi k/(N\alpha)$ for $1 \leqslant k \leqslant N$ and $Q = 2\pi l/\alpha$ for $l \in \mathbb{Z}$. With this,

$$\begin{aligned}&\boldsymbol{\varepsilon}_j^\dagger \nabla_{\boldsymbol{\rho}_0} \Phi(\boldsymbol{\rho}_0, \sigma) \\ &= \frac{1}{N\alpha}\frac{1}{\sqrt{N}} \sum_n \sum_{q,Q} i(q+Q) \\ &\quad \times e^{-\frac{2\pi i j n}{N}} e^{-i(q+Q)(\sigma - \alpha n)} \Phi_{q+Q} \\ &= \frac{1}{\alpha\sqrt{N}} \sum_Q i\left(\frac{2\pi j}{N\alpha} + Q\right) e^{-i\left(\frac{2\pi j}{N\alpha} + Q\right)\sigma} \Phi_{\frac{2\pi j}{N\alpha} + Q}, \end{aligned} \tag{20}$$

where we perform the summation over n before the one over q, turning Eq. (18) into

$$\begin{aligned}\zeta_j(\tau_*) =& -\frac{2\pi\cos(2\pi\omega_j\tau_*)}{\alpha\sqrt{N}}\sqrt{\frac{\hbar}{\Omega_{\text{slow}}}} \int_{-\tau_*}^{\tau_*} d\tau \frac{e^{-2\pi i\omega_j\tau}}{\omega_j} \\ &\times \sum_Q \left(\frac{2\pi j}{N\alpha} + Q\right) e^{-i\left(\frac{2\pi j}{N\alpha} + Q\right)\sigma} \Phi_{\frac{2\pi j}{N\alpha} + Q}. \end{aligned} \tag{21}$$

Next, we assume that the kinetic energy of the mobile particle is substantially larger than the variation of the potential profile produced by the chain. This is a reasonable assumption because, once the two energy scales become comparable, the mobile particle is expected to get trapped in a potential minimum very shortly. Since we are interested in the dissipation during the particle's motion along the chain, we will focus on the portion of the trajectory sufficiently far from the trapping. This simplification allows us to view the particle's speed as approximately constant, writing $\sigma(\tau) \to \dot{\sigma}\tau$. Integrating over τ in Eq. (21) yields

$$\begin{aligned}\zeta_j(\tau_*) =& -\frac{2\pi}{\alpha\sqrt{N}}\sqrt{\frac{\hbar}{\Omega_{\text{slow}}}} \frac{\cos(2\pi\omega_j\tau_*)}{\omega_j} \sum_l \left(\frac{2\pi j}{N\alpha} + \frac{2\pi l}{\alpha}\right) \\ &\times \Phi_{\frac{2\pi j}{N\alpha} + \frac{2\pi l}{\alpha}} \frac{2\sin\left\{\tau_*\left[2\pi\omega_j + \left(\frac{2\pi j}{N\alpha} + \frac{2\pi l}{\alpha}\right)\dot{\sigma}\right]\right\}}{2\pi\omega_j + \left(\frac{2\pi j}{N\alpha} + \frac{2\pi l}{\alpha}\right)\dot{\sigma}}. \end{aligned} \tag{22}$$

Equation (22) gives the amplitude A_j of the jth mode, which is related to the mode's energy via $E_j = \Omega_{\text{slow}}^2\omega_j^2 A_j^2/2$. In terms of E_{slow}, this energy becomes

$$\begin{aligned}\mathcal{E}_j =& \frac{1}{2N}\left[\frac{2\pi}{\alpha}\sum_l \left(\frac{2\pi j}{N\alpha} + \frac{2\pi l}{\alpha}\right)\Phi_{\frac{2\pi j}{N\alpha} + \frac{2\pi l}{\alpha}}\right. \\ &\left.\times \frac{2\sin\left\{\tau_*\left[2\pi\omega_j + \left(\frac{2\pi j}{N\alpha} + \frac{2\pi l}{\alpha}\right)\dot{\sigma}\right]\right\}}{2\pi\omega_j + \left(\frac{2\pi j}{N\alpha} + \frac{2\pi l}{\alpha}\right)\dot{\sigma}}\right]^2. \end{aligned} \tag{23}$$

Summing Eq. (23) over j gives the amount of energy transferred from the mobile particle to the chain during the interval $2\tau_*$.

V. SINGLE-PASS DISSIPATION

To explore the dissipation's dependence on system parameters, we now develop an analytical model of energy loss when the mobile particle passes a single chain mass. Setting $\tau_* = \alpha/2\dot{\sigma}$ in Eq. (23) gives the energy dissipated by the moving particle after passing a single chain mass:

$$\begin{aligned}\mathcal{E}_j &= \frac{1}{2N}\left[\frac{2\pi}{\alpha}\sum_l \left(\frac{2\pi j}{N\alpha} + \frac{2\pi l}{\alpha}\right)\Phi_{\frac{2\pi j}{N\alpha} + \frac{2\pi l}{\alpha}} \frac{2\sin\left\{\frac{\alpha}{2\dot{\sigma}}\left[2\pi\omega_j + \left(\frac{2\pi j}{N\alpha} + \frac{2\pi l}{\alpha}\right)\dot{\sigma}\right]\right\}}{2\pi\omega_j + \left(\frac{2\pi j}{N\alpha} + \frac{2\pi l}{\alpha}\right)\dot{\sigma}}\right]^2 \\ &\overset{\alpha\to\infty}{=} \frac{1}{2N}\left[\int_{-\infty}^{\infty}\frac{dx}{\dot{\sigma}}\left(\frac{2\pi j}{N\alpha} + x\right)\Phi_{\frac{2\pi j}{N\alpha} + x} \frac{2\sin\left[\frac{\alpha}{2}\left(\frac{2\pi\omega_j}{\dot{\sigma}} + \frac{2\pi j}{N\alpha} + x\right)\right]}{\frac{2\pi\omega_j}{\dot{\sigma}} + \frac{2\pi j}{N\alpha} + x}\right]^2 \\ &\overset{\alpha\to\infty}{=} \frac{1}{2N}\left[\frac{2\pi}{\dot{\sigma}}\left(\frac{2\pi\omega_j}{\dot{\sigma}}\right)\Phi_{\frac{2\pi\omega_j}{\dot{\sigma}}}\right]^2. \end{aligned} \tag{24}$$

The $\alpha \to \infty$ limit is applicable if the separation between the chain masses α is substantially larger than the characteristic width of the interaction term $\Phi(x)$ so the particle interacts with only one chain mass at a time. For an arbitrary interaction Φ which approaches zero at large separations, assuming the chain displacements vanish (justified by the small $\delta\rho$ seen in Fig. 3), and taking the limit $\alpha \to \infty$, we obtain a single-pass dissipation:

$$\Delta = \sum_j \frac{1}{2N}\left[\frac{4\pi^2\omega_j}{\dot\sigma^2}\int du\, \exp\left(i\frac{2\pi\omega_j}{\dot\sigma}u\right)\Phi(u)\right]^2. \quad (25)$$

In the high-velocity limit, $\dot\sigma \to \infty$, the Fourier transform inside the square brackets approaches $\int dx\, \Phi(x)$ as the exponential function tends to 1. If the integral is convergent, we find $\Delta \propto \dot\sigma^{-4}$. Given that the frequency of encounters between the mobile particle and the chain masses is proportional to $\dot\sigma$, we multiply the energy loss per pass by the speed to obtain the energy dissipation rate: $\Delta\dot\sigma \sim \dot\sigma^{-3}$. In between interactions with the chain masses, the mobile particle's total energy $\mathcal{E}$ is proportional to $\dot\sigma^2$, so the energy loss rate $\dot{\mathcal{E}} \sim -\mathcal{E}^{-3/2}$ produces a quasi-power-law decay of the energy. If the integral in Eq. (25) is not convergent (such as in the case of Coulomb interaction), the divergence will be mitigated by the faster-decaying $\dot\sigma^{-4}$ prefactor, also leading to quasi-power-law energy decay. Crucially, unlike typical drag, where faster motion produces more resistance by the medium, higher speed here actually results in reduced dissipation.

Physically, the decrease in dissipation with increasing speed can be understood by considering the displacement of the chain mass due to its interaction with the incident particle. Let the average force that the chain mass experiences during the interaction be $\bar f$ and the effective interaction time be $\tau_{\rm int}$. The displacement of the chain mass arising from the interaction then becomes $\sim \bar f \tau_{\rm int}^2$. The potential energy stored in the compressed springs due to the mass's displacement is proportional to the displacement squared and, hence, to $\tau_{\rm int}^4$. The effective interaction time $\tau_{\rm int} \sim \lambda/\dot\sigma$, so the elastic energy originating from the particle's kinetic energy is proportional to $\dot\sigma^{-4}$, which is the scaling of Δ at large speeds.

For small $\dot\sigma$, the behavior is strongly dependent on the potential profile. For a nondiverging potential, the Fourier term in Eq. (25) vanishes because small $\dot\sigma$ corresponds to a high Fourier momentum. Consequently, for $\dot\sigma \lesssim \omega_j\Lambda$, where Λ is the characteristic width of the potential, the chain mode does not absorb energy from the moving particle. If $\dot\sigma \lesssim \omega_j\Lambda$ for all the modes in the chain (which is possible for a gapped spectrum considered here), the particle experiences essentially no dissipation. For singular potentials, the Fourier term diverges as a logarithm or a power of $2\pi\omega_j/\dot\sigma$, resulting in a (quasi-)power-law dependence of Δ on $1/\dot\sigma$, also leading to a power-law-like decay of energy with time. More importantly, diverging potentials are not allowed in the 1D case because the mobile particle cannot circumvent them, making any discussion of it passing a chain mass inapplicable. Conceptually, if the particle is moving slowly compared to a mode frequency, the mode manages to return some of its energy to the mobile particle. Hence, the nonmonotonicity of Δ for a system with hard phonon modes can be seen as a competition between the reduced interaction time at high speeds and the reduced number of modes participating in the dissipation at low speeds. We emphasize that, despite the exponential suppression of dissipation at low speeds, the motion is never fully dissipationless. Such suppressed dissipation might be of interest to researchers working on polarons in solid-state systems [45].

As a concrete example, we consider a Gaussian interaction, as in Fig. 3, for which the sum in Eq. (25) can be computed analytically, yielding

$$\Delta = 4\pi^3\frac{\Phi_0^2}{\dot\sigma^2}\left(\frac{2\pi\lambda}{\dot\sigma}\right)^2 e^{-\left(\frac{2\pi\lambda}{\dot\sigma}\right)^2(\omega_{\rm fast}^2+1)/2} \times\left\{I_0(W)+\frac{\omega_{\rm fast}^2-1}{2}[I_0(W)-I_1(W)]\right\}, \quad (26)$$

where $W \equiv (\frac{2\pi\lambda}{\dot\sigma})^2(\omega_{\rm fast}^2-1)/2$, and I_n are modified Bessel functions of the first kind. In the fast mobile particle limit, $\dot\sigma \gg 2\pi\lambda\omega_{\rm fast}$,

$$\Delta_{\rm fast} = 2\pi^3\frac{\Phi_0^2}{\dot\sigma^2}\left(\frac{2\pi\lambda}{\dot\sigma}\right)^2\left(\omega_{\rm fast}^2+1\right), \quad (27)$$

recovering the expected power law. Conversely, for small values of $\dot\sigma$, the single-pass dissipation is exponentially suppressed:

$$\Delta_{\rm slow} = 4\pi^3\frac{\Phi_0^2}{\dot\sigma^2}\left(\frac{2\pi\lambda}{\dot\sigma}\right)e^{-\left(\frac{2\pi\lambda}{\dot\sigma}\right)^2}\frac{1}{\sqrt{\pi\left(\omega_{\rm fast}^2-1\right)}}. \quad (28)$$

The analytic form of single-pass dissipation can be seen in Fig. 5, plotted for various interaction potentials in both low- and high-velocity limits. To numerically validate the approximations made deriving Eq. (25), we initialize the mobile particle with various velocities $\dot\sigma_0$ halfway between two masses of a chain that is initially at rest. We evolve the system for a time $\tau = 1.25\times\alpha/\dot\sigma_0$ using the equations of motion (12)–(14). This time is long enough for the mobile particle to pass a single chain mass and reach the next midpoint, at which we calculate the kinetic energy $T = M\dot R^2/2 = \hbar\Omega_{\rm slow}(2\pi)^{-2}\mu\dot\sigma^2/2$ and subtract it from the initial kinetic energy. We used different simulation parameters for the low- and high-$\dot\sigma$ regimes to avoid some technical issues. For slow speeds, Φ_0 must be smaller than the kinetic energy associated with the minimum value of $\dot\sigma$ to prevent the particle from getting stuck in the case of a repulsive interaction. Using the same Φ_0 for fast speeds is problematic, however, as $\Delta_{\rm fast} \propto \Phi_0^2$ becomes an exceedingly small fraction of the initial kinetic energy, leading to numerical issues when subtracting $T(\tau) - T(0)$. Hence, we calculated the low- and high-$\dot\sigma_0$ behavior using different values of $|\Phi_0|$.

The resulting energy losses Δ agree well with the analytical predictions, as shown in Fig. 5. For each set of parameters, the attractive ($\Phi_0 < 0$) and repulsive ($\Phi_0 > 0$) cases shift toward lower and higher $\dot\sigma_0$, respectively. The reason behind this shift has to do with the fact that the analytic formula $\Delta(\dot\sigma_0)$ assumes a constant particle speed, which is not strictly true as the particle accelerates near the chain mass for $\Phi_0 < 0$ and decelerates for $\Phi_0 > 0$, as discussed in Sec. IV A. As a first approximation, we can consider the average effective velocity for each case, which is lower (higher) than $\dot\sigma_0$ for the repulsive (attractive) case. This explains both the directions of these deviations and the fact that magnitude of these deviations

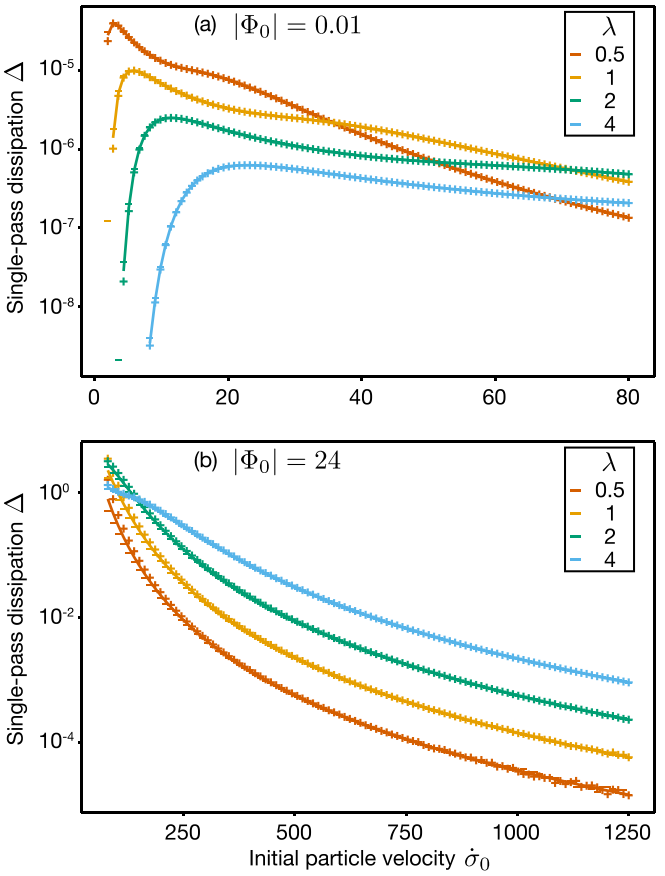

FIG. 5. *Single-pass dissipation.* Energy loss Δ for low velocity (a) with $|\Phi_0| = 1/100$, and high velocity (b) with $|\Phi_0| = 24$. The solid lines are analytical calculations using Eq. (26) for different values of λ. The "+" and "−" symbols show the numerical values of Δ obtained from single-pass trajectories, where the symbols correspond to repulsive ($\Phi_0 > 0$) and attractive ($\Phi_0 < 0$) potentials respectively.

increases as $\dot{\sigma}_0$ decreases. The difference between the two interaction signs is more pronounced when Φ_0 is comparable to the kinetic energy of the particle, as shown in Fig. 6.

Eliminating the $\alpha \to \infty$ approximation means that the argument inside the brackets of the sine function and the denominator in Eq. (23) cannot be made to vanish for any $\dot{\sigma}$ for a particular j. Instead, this expression goes to zero only for speeds which satisfy $\dot{\sigma} = \alpha\omega_j/(\frac{j}{N} + l)$. For these speeds, $\mathcal{E}_j \propto \tau_*^2$, leading to an enhanced excitation of the jth mode. If the density of states is high around the jth mode, this enhanced excitation will lead to an increased dissipation by the mobile particle. Because the density of states is highest at the band edges due to the van Hove singularities, we expect this enhancement to be most consequential for ω_{slow} and ω_{fast}. For ω_{slow}, $j = 1$ and the speeds become $\dot{\sigma} = \alpha\omega_{\text{slow}}/l = \alpha/l$ with $l > 0$, since $l = 0$ is excluded due to the vanishing prefactor. For ω_{fast}, $j = N/2$ and the speeds become $\dot{\sigma} = 2\alpha\omega_{\text{fast}}/(2l + 1)$ with $l \geqslant 0$.

To visualize the effect of this increased dissipation, we plot the energy losses Δ (during the full particle trajectories of Fig. 3) in Fig. 7. We also plot vertical lines at $\dot{\sigma} = 2\alpha\omega_{\text{fast}}/(2l + 1)$ to indicate the speeds at which we expect to see an enhanced dissipation due to the states at the top of

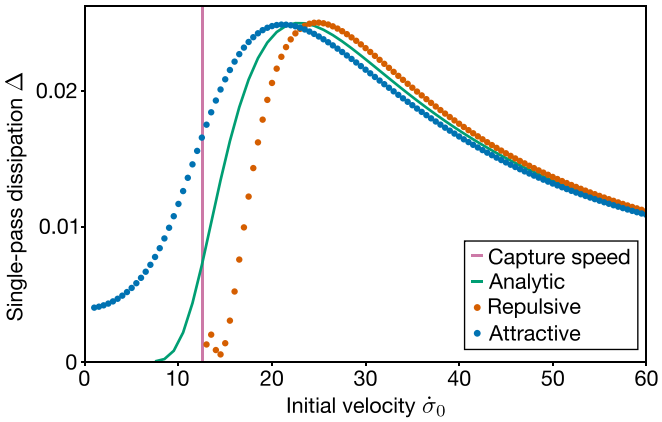

FIG. 6. *Dissipation after passing single chain mass.* Energy losses Δ for a range of initial particle velocities. The green solid line is the analytic curve calculated using Eq. (26) and the circle symbols show numerical Δ values obtained from single-pass trajectories for both repulsive and attractive cases. The mobile particle is initialized halfway between chain masses and the parameters used are $\alpha = 40$, $\Phi_0 = \pm 2$, $\lambda = 4$, $\omega_{\text{fast}} = 10$, and $\mu = 1$. The vertical line indicates the minimum velocity required to overcome the potential barrier for the repulsive case, as discussed in Sec. IV A.

the mode band. We observe peaks in Δ close to the vertical lines, followed by an oscillatory behavior as $\dot{\sigma}_0$ is reduced. The enhancement is strongest for the largest velocity with the higher-l peaks being much weaker. In addition, we observe a shift toward higher (lower) velocities for attractive (repulsive) potentials due to the velocity fluctuation discussed in Sec. IV A.

VI. STEADY-STATE DISSIPATION

To study the long-time dynamics of the system, we consider dissipation in the steady-state limit when the mobile particle passes all N chain masses, and $N \to \infty$. We first take

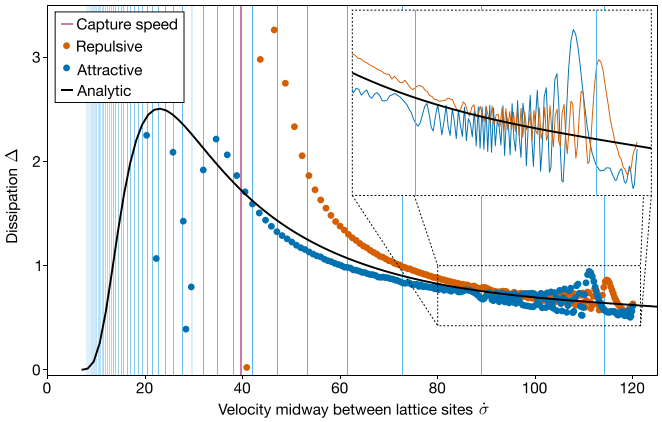

FIG. 7. *Dissipation along full trajectory.* Energy losses Δ calculated from the trajectories plotted in Fig. 3 (circles) and from Eq. (26) (black curve). We plot speeds at which dissipation is predicted to be enhanced at $\dot{\sigma} = 2\alpha\omega_{\text{fast}}/(2l + 1)$ (blue vertical lines). Inset: Zoomed-in plot at high speeds to highlight oscillatory behavior of Δ.

$\tau_* = N\alpha/2\dot{\sigma}$ and Eq. (23) becomes

$$\mathcal{E}_j = \frac{1}{2N}\left[\frac{2\pi}{\alpha}\sum_l \left(\frac{2\pi j}{N\alpha}+\frac{2\pi l}{\alpha}\right)\Phi_{\frac{2\pi j}{N\alpha}+\frac{2\pi l}{\alpha}} \times \frac{2\sin\left\{\frac{N\alpha}{2\dot{\sigma}}\left[2\pi\omega_j+\left(\frac{2\pi j}{N\alpha}+\frac{2\pi l}{\alpha}\right)\dot{\sigma}\right]\right\}}{2\pi\omega_j+\left(\frac{2\pi j}{N\alpha}+\frac{2\pi l}{\alpha}\right)\dot{\sigma}}\right]^2, \tag{29}$$

corresponding to energy absorbed by the jth chain mode after a mobile particle traverses the entire system at speed $\dot{\sigma}$. Naturally, for $N\to\infty$, summing Eq. (29) over j results in a diverging quantity. However, dividing the sum by N gives the energy absorbed by the chain for each chain mass passed by the particle:

$$\begin{aligned}\bar{\Delta} &= \lim_{N\to\infty}\frac{1}{N}\sum_j \frac{1}{2N}\left[\frac{2\pi}{\alpha}\sum_l \left(\frac{2\pi j}{N\alpha}+\frac{2\pi l}{\alpha}\right)\Phi_{\frac{2\pi j}{N\alpha}+\frac{2\pi l}{\alpha}}\frac{2\sin\left\{\frac{N\alpha}{2\dot{\sigma}}\left[2\pi\omega_j+\left(\frac{2\pi j}{N\alpha}+\frac{2\pi l}{\alpha}\right)\dot{\sigma}\right]\right\}}{2\pi\omega_j+\left(\frac{2\pi j}{N\alpha}+\frac{2\pi l}{\alpha}\right)\dot{\sigma}}\right]^2 \\ &= \lim_{N\to\infty}\frac{1}{2N^2}\left(\frac{2\pi}{\alpha}\right)^2\sum_{jll'}\left(\frac{2\pi j}{N\alpha}+\frac{2\pi l}{\alpha}\right)\Phi_{\frac{2\pi j}{N\alpha}+\frac{2\pi l}{\alpha}}\frac{2\sin\left\{\frac{N\alpha}{2\dot{\sigma}}\left[2\pi\omega_j+\left(\frac{2\pi j}{N\alpha}+\frac{2\pi l}{\alpha}\right)\dot{\sigma}\right]\right\}}{2\pi\omega_j+\left(\frac{2\pi j}{N\alpha}+\frac{2\pi l}{\alpha}\right)\dot{\sigma}} \\ &\quad\times\left(\frac{2\pi j}{N\alpha}+\frac{2\pi l'}{\alpha}\right)\Phi_{\frac{2\pi j}{N\alpha}+\frac{2\pi l'}{\alpha}}\frac{2\sin\left\{\frac{N\alpha}{2\dot{\sigma}}\left[2\pi\omega_j+\left(\frac{2\pi j}{N\alpha}+\frac{2\pi l'}{\alpha}\right)\dot{\sigma}\right]\right\}}{2\pi\omega_j+\left(\frac{2\pi j}{N\alpha}+\frac{2\pi l'}{\alpha}\right)\dot{\sigma}}.\end{aligned} \tag{30}$$

In the limit $N\to\infty$, the two fractions with sine in the numerator become nascent Dirac delta functions. Consequently, $l = l'$ for the expression not to vanish,

$$\begin{aligned}\bar{\Delta} &= \lim_{N\to\infty}\frac{1}{2N^2}\left(\frac{2\pi}{\alpha}\right)^2\sum_{jl}\left[\left(\frac{2\pi j}{N\alpha}+\frac{2\pi l}{\alpha}\right)\Phi_{\frac{2\pi j}{N\alpha}+\frac{2\pi l}{\alpha}}\frac{2\sin\left\{\frac{N\alpha}{2\dot{\sigma}}\left[2\pi\omega_j+\left(\frac{2\pi j}{N\alpha}+\frac{2\pi l}{\alpha}\right)\dot{\sigma}\right]\right\}}{2\pi\omega_j+\left(\frac{2\pi j}{N\alpha}+\frac{2\pi l}{\alpha}\right)\dot{\sigma}}\right]^2 \\ &= \lim_{N\to\infty}\frac{1}{2N^2}\left(\frac{2\pi}{\alpha}\right)^2\sum_{k=-\infty}^{\infty}\left[\frac{2\pi k}{N\alpha}\Phi_{\frac{2\pi k}{N\alpha}}\frac{2\sin\left[\frac{N\alpha}{2\dot{\sigma}}\left(2\pi\omega_k+\frac{2\pi k}{N\alpha}\dot{\sigma}\right)\right]}{2\pi\omega_k+\frac{2\pi k}{N\alpha}\dot{\sigma}}\right]^2 \\ &= \int_{-\infty}^{\infty}dx\left(\frac{2\pi}{\alpha}\right)^2\left(\frac{2\pi}{\alpha}x\Phi_{\frac{2\pi}{\alpha}x}\right)^2\lim_{N\to\infty}\frac{2}{N}\left[\frac{\sin\left[\frac{N\alpha}{2\dot{\sigma}}\left(2\pi\omega(x)+\frac{2\pi}{\alpha}\dot{\sigma}x\right)\right]}{2\pi\omega(x)+\frac{2\pi}{\alpha}\dot{\sigma}x}\right]^2,\end{aligned} \tag{31}$$

where $\omega(x) = \sqrt{1+(\omega_{\text{fast}}^2-1)\sin^2(\pi x)}$. Taking the limit turns the expression inside the brackets into a Dirac delta function:

$$\begin{aligned}\bar{\Delta} &= \frac{2}{N}\int_{-\infty}^{\infty}dx\left(\frac{4\pi^2}{\alpha^2}x\Phi_{\frac{2\pi}{\alpha}x}\right)^2\pi\frac{N\alpha}{2\dot{\sigma}}\delta\left[2\pi\omega(x)+\frac{2\pi}{\alpha}x\dot{\sigma}\right] \\ &= \int_{-\infty}^{\infty}dx\left(\frac{4\pi^2}{\alpha^2}x\Phi_{\frac{2\pi}{\alpha}x}\right)^2\frac{\alpha}{2\dot{\sigma}}\delta\left[\omega(x)+\frac{x\dot{\sigma}}{\alpha}\right].\end{aligned} \tag{32}$$

If x_j are the solutions to $\omega(x)+\frac{x\dot{\sigma}}{\alpha}=0$, we have

$$\begin{aligned}\bar{\Delta} &= \sum_j\left(\frac{4\pi^2}{\alpha^2}x_j\Phi_{\frac{2\pi}{\alpha}x_j}\right)^2\frac{\alpha}{2\dot{\sigma}}\frac{1}{\left|\omega'(x_j)+\frac{\dot{\sigma}}{\alpha}\right|} \\ &= \frac{1}{2}\sum_j\left[\frac{4\pi^2\omega(x_j)}{\dot{\sigma}^2}\Phi_{\frac{2\pi\omega(x_j)}{\dot{\sigma}}}\right]^2\frac{1}{|\alpha\omega'(x_j)/\dot{\sigma}+1|}.\end{aligned} \tag{33}$$

Equation (33) tells us that, in a long-time limit, only certain chain modes absorb energy from the mobile particle, while the net energy exchange with all other modes vanishes. Moreover, if $-x\dot{\sigma}/\alpha$ has a slope similar to the phonon band at x_s, the denominator in Eq. (33) becomes small and $\bar{\Delta}$ acquires a peak. Because x_s does not have to lie in the first Brillouin zone, $\bar{\Delta}$ can have multiple peaks originating from different Brillouin zones, similar to an Umklapp process. The slope matching occurs when $-x_s\dot{\sigma}/\alpha \approx 1 = \omega_{\text{slow}}$, near the bottom band edge, so the corresponding speeds are given by $\dot{\sigma}\approx\alpha/n$ for all positive integers n. We confirm the existence of these peaks by plotting Eq. (33) in Fig. 8(c).

To emulate conduction in macroscopic devices, we additionally introduce a bias term in the form of a constant gradient in the potential experienced by the mobile particle. This bias has the effect of increasing the mobile particle's kinetic energy by a fixed amount β after each pass, which can counteract the energy $\bar{\Delta}$ dissipated to the chain. When $\bar{\Delta}(\dot{\sigma})-\beta=0$, a mobile particle will have velocity $\dot{\sigma}$ both before and after passing each chain mass. This behavior will lead to a constant average velocity, akin to a drift velocity in conducting materials.

For a mobile particle moving with $\bar{\Delta}$ just above one of the spikes, a positive value of $\bar{\Delta}(\dot{\sigma})-\beta$ will cause the particle's velocity to decrease below the spike, and for velocity just below a spike, interaction with the chain and the bias will cause the particle's velocity to increase. These behaviors lead to stable points in the vicinity of $\dot{\sigma}=\alpha/n$. Corresponding to each spike is another, higher velocity that satisfies $\bar{\Delta}(\dot{\sigma})-\beta=0$. For velocities slightly higher (lower) than these solutions, the particle $\bar{\Delta}(\dot{\sigma})-\beta$ is negative (positive), so the particle's velocity will increase (decrease), leading to an unstable repulsive point. The existence of multiple stable points due to the multiple spikes indicates that, for a given bias, there are multiple drift velocities.

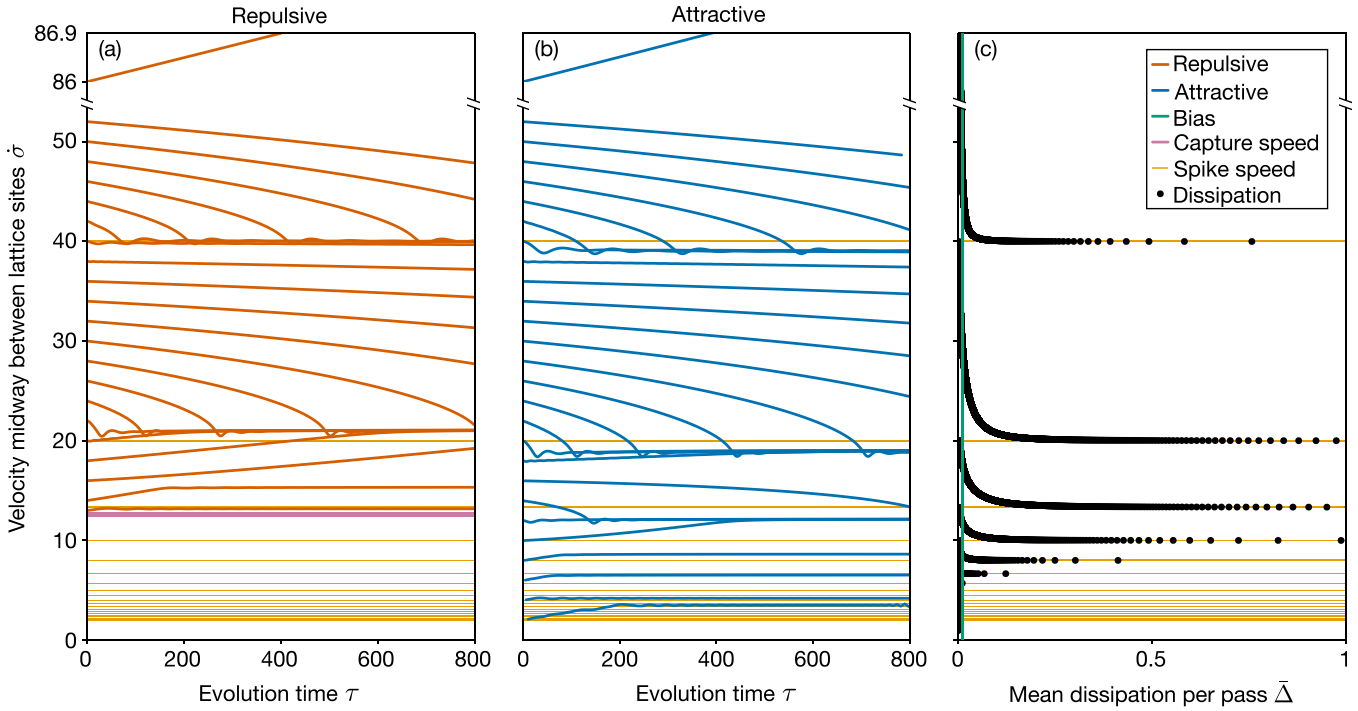

FIG. 8. *Multiple drift velocities maintained by constant bias.* The evolution of particle speeds for a range of initial speeds for system parameters $\alpha = 40$, $\Phi_0 = \pm 2$, $\lambda = 4$, and bias $\beta = 0.01$ for repulsive interactions (a) and attractive interactions (b). For clarity, we plot local maxima (minima) for repulsive (attractive) interactions and neglect the interaction-induced velocity fluctuation (see Sec. IV A for details). The horizontal orange lines show velocities α/n, where n is a positive integer, corresponding to spikes in $\bar{\Delta}$. For the repulsive case, the minimum speed required to overcome the potential barrier (the capture speed) is given by $8\pi^2\Phi_0/\mu \approx 12.6$. Small bias leads to a very modest acceleration at high speeds, so we use a different scale to demonstrate a positive slope of the curve. (c) shows the mean dissipation per pass $\bar{\Delta}$ in the steady-state limit.

To confirm the unusual presence of these drift velocities, we perform numerical simulations of particle trajectories for a range of initial speeds, for both repulsive and attractive interactions in the presence of a bias. Figures 8(a) and 8(b) plot the evolution of particle speeds with time and the spike locations, $\dot{\sigma} = \alpha/n$, are marked by horizontal lines. We can see that the computed trajectories fall into three categories. For high enough $\dot{\sigma}_0$, the dissipation is always smaller than the bias, and the particle accelerates away. For intermediate velocities, the particle can accelerate or decelerate depending on the initial speed to a drift velocity near α/n. For the repulsive case, particles with $\dot{\sigma}_0$ below the capture velocity are trapped by the chain, having insufficient kinetic energy to go over the potential energy maximum. As predicted by our analytics, we see that multiple drift velocities are supported in both the repulsive and attractive cases.

As discussed in Secs. IV A and V, the particle does not move at a constant velocity throughout its trajectory, leading to moderate deviations from these predictions. Near each chain mass, an attractive (repulsive) potential leads to an increase (decrease) in the particle velocity, so the velocity takes a range of values (see Fig. 6). This velocity fluctuation has the effect of broadening the spikes of Fig. 8(c), making $\bar{\Delta}$ finite at the orange lines $\dot{\sigma} = \alpha/n$ instead of diverging; see Fig. 9. This broadening will shift both the stable drift velocities and unstable solutions toward lower (higher) velocities for the attractive (repulsive) case. In addition to shifting the spikes' locations, velocity fluctuations cause them to overlap, so $\bar{\Delta}(\dot{\sigma}) - \beta = 0$ is not satisfied for low $\dot{\sigma}$. To compute this broadened $\bar{\Delta}$, we average over $\dot{\sigma} \in [\dot{\sigma}_0, \dot{\sigma}_{\text{ext}}]$. Instead of

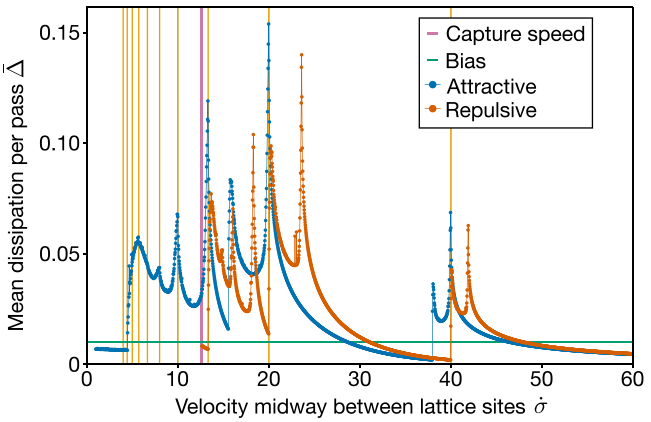

FIG. 9. *Broadened mean dissipation per pass.* Broadened $\bar{\Delta}$ for the parameters of Fig. 8 calculated using Eq. (33) and weighted over velocity fluctuations. The vertical orange lines show $\dot{\sigma} = \alpha/n$ for positive integers $1 \leqslant n \leqslant 10$, indicating velocities at which we expect an enhanced dissipation. The pink vertical line shows the predicted minimum velocity for the repulsive case. The horizontal green line indicates the bias value used in the trajectories plotted in Figs. 8(a) and 8(b). At low velocities, this broadening effectively removes the spikes in $\bar{\Delta}$, which predicts a smaller number of drift velocities than shown in our numerical simulations.

assuming equal weights over the velocity range, we compute the probability distribution of speeds of the mobile particle as it moves from one point midway between two chain masses to the next. After this, we use the weights of this distribution to perform an averaging of $\bar{\Delta}$ in the range $[\dot{\sigma}_0, \dot{\sigma}_{\text{ext}}]$. Considering the velocity fluctuation also makes $\bar{\Delta}$ dependent on the sign of the interaction potential and reveals the same shifts to the right (left) for the repulsive (attractive) case as seen in Sec. V. For repulsive potentials, another drift velocity exists at low $\dot{\sigma}$ where the mobile particle almost comes to rest during each pass. These solutions have velocity just above the capture velocity of the chain. Additionally, at lower speeds, when the fluctuation magnitude becomes comparable to the drift velocity, the deviation from α/n is more pronounced. As we can see from Figs. 8(a) and 8(b), this broadening predicts fewer drift velocities than observed in the numerics. This is likely due to the oversimplification of assuming a constant speed in the derivation of $\bar{\Delta}$. For this reason, Fig. 9 serves as a qualitative illustration of how velocity variation modifies the dissipation in steady state and should not be taken as a quantitative prediction.

Experimentally, an observed drift velocity in a 1D ionic conductor would serve as a probe of effective chain parameters. Since the highest $\dot{\sigma}_{\text{drift}} \approx \alpha = a/\sqrt{\hbar/\sqrt{\kappa m}}$, where the chain spacing a can be directly measured, $\dot{\sigma}_{\text{drift}}$ indirectly measures the product of the chain mass and its confinement. A realistic system, however, will experience thermal motion of the chain masses, which will further blur the spikes in $\bar{\Delta}$. We will explore the role of these thermal fluctuations in future work.

In the absence of thermal fluctuations, our model qualitatively relies on only two energy scales: the strength of the interaction between the particle and the framework Φ_0 and the maximum energy of the phonon band ω_{fast}. In solid electrolytes, numerical calculations of the lithium migration barrier indicate $\Phi_0 \sim 100\,\text{meV}$ [11,18]. In LISICON electrolytes, the potential energy profile is similar to the Lennard-Jones form, with $\Phi_0 \sim -5 \pm 1\,\text{eV}$, depending on the tetrahedral $(XO_4)^{m-}$ group (where X is Al, Si, Ge, or P) [19]. For carbon nanotubes, on the other hand, the minimum of the interaction energy between a copper atom inside the nanotube and one of the carbons gives $\Phi_0 \sim -0.14\,\text{eV}$. [32] Because the maximum phonon energy in a crystal is typically 10 to 30 THz [46], corresponding to $O(0.1\,\text{eV})$, the magnitude of the interaction is generally larger than the energy of the highest-energy phonon. In other words, Φ_0 is generally greater than ω_{fast}, but the precise ratio can vary widely.

VII. SUMMARY

We considered the 1D motion of a single mobile particle that interacts with each mass in an infinite chain via a nonlinear coupling. We showed, using numerical simulations and a simplified single-pass model, that this interaction will dissipate the mobile particle's energy until it is trapped by the chain. Unlike typical drag, this dissipation rate is reduced at higher speeds. We also introduced a bias term, and using a steady-state model and numerical simulations, found that the resulting dynamics show a variety of behaviors. The mobile particle can exhibit runaway acceleration and can be trapped by the chain masses, but it can also settle into one of multiple stable drift velocities determined by chain parameters. Signatures of these dynamics should be measurable in conduction channels where the motion is effectively 1D, such as electrons, simple molecules, and fullerenes in carbon nanotubes, or ions in anisotropic crystals.

ACKNOWLEDGMENTS

A.R. acknowledges the National Research Foundation, Prime Minister Office, Singapore, under its Medium Sized Centre Programme and the support by Yale-NUS College (through Start-up Grant). B.A.O. acknowledges support from the Ministry of Education and Yale-NUS College (through Start-up grant and Grant Nos. IG20-SG102 and IG20-SI101). H.M. is supported by the Ministry of Education, Singapore, under its Research Centre of Excellence award to the Institute for Functional Intelligent Materials (I-FIM, Project No. EDUNC-33-18-279-V12). The computational work involved in this project was partially supported by NUS IT Research Computing Group.

B.A.O. and A.R. conceptualized the work; H.M. and A.R. wrote the code which was used by them and Z.W.Y. to run the simulations; H.M., B.A.O., and A.R. analyzed the results, prepared the graphics, and wrote the manuscript.

APPENDIX: COMPUTATIONAL PROCEDURE

In the most general sense, Eqs. (12) and (14) are solved numerically by first rewriting them as discrete difference equations for time step δ:

$$\boldsymbol{\rho}_\beta = \sum_j \boldsymbol{\varepsilon}_j \sqrt{n_j + \frac{1}{2}}\sqrt{\frac{2}{\omega_j}} \cos(2\pi\omega_j\delta\beta + \phi_j) - 2\pi\delta \sum_\gamma \overleftrightarrow{\Gamma}[\delta(\beta-\gamma)]\nabla_{\boldsymbol{\rho}}\Phi(\boldsymbol{\rho}_\gamma, \boldsymbol{\sigma}_\gamma), \tag{A1}$$

$$\sigma_{j,\beta} = -\frac{(2\pi\delta)^2}{\mu}\sum_k \frac{d\Phi(\rho_{k,\beta-1}, \sigma_{j,\beta-1})}{d\sigma_j} + 2\sigma_{j,\beta-1} - \sigma_{j,\beta-2}, \tag{A2}$$

where β and γ are time step labels. The solution is obtained iteratively, after initializing $\sigma_{0,j}$ and $\sigma_{1,j} = \sigma_{0,j} + \delta\dot{\sigma}_{0,j}$, where $\dot{\sigma}_{0,j}$ is the initial velocity of the mobile particle. Despite the fairly standard computing protocol, calculating the trajectories efficiently and reliably requires some care.

First, we clearly cannot solve the problem for an infinitely large system, so $\boldsymbol{\rho}$ has to be a finite vector. Therefore, we pick a segment of the chain with N_{ch} masses whose positions will be tracked. As long as the mobile particles remain within this segment, all the interactions between them and the *infinitely long* chain will be accounted for. The trajectories of the chain masses are saved to a $N_{\text{ch}} \times N_{\text{step}}$ matrix $\overleftrightarrow{\rho}$, where N_{step} is the number of time steps in the simulation. Similarly, the trajectories of the mobile particles are saved in a $N_{\text{particle}} \times N_{\text{step}}$ matrix $\overleftrightarrow{\sigma}$, where N_{particle} is the number of particles in the system. Prior to the simulation, $\overleftrightarrow{\rho}$ is filled with the mass trajectories originating from the thermal motion of the chain, which are all zeros in this case. During the simulation, it is

updated in accordance with the second term of Eq. (A1) in a manner discussed below.

To guarantee the smoothness of the chain response, δ has to be much smaller than the shortest timescale intrinsic to the chain, corresponding to the fastest chain mode Ω_{fast}. Hence, we choose δ to be much smaller than this mode's period $\tau_{\text{fast}} = (2\pi/\Omega_{\text{fast}})/(2\pi/\Omega_M) = 1/\omega_{\text{fast}}$. In our earlier work [44], we found that $\delta = 1/60\omega_{\text{fast}}$ is sufficiently small and we employ this value of δ here, unless otherwise specified. The second point to consider when choosing δ involves the particle-chain interaction. To avoid numerical artifacts, the time step has to be substantially smaller than the particle-chain interaction time. In other words, $\delta\dot{\sigma} \ll \Lambda$, where Λ is the characteristic interaction length. Therefore, we will take care to ensure that for a fixed δ, the interaction term remains sufficiently wide and the particle speed is kept sufficiently low.

With δ expressed in terms of the fastest chain mode, we need to decide on the magnitude of ω_{fast}. We see that a single period of the slowest mode $\tau = 1$ contains $1/\delta = 60\omega_{\text{fast}}$ time steps and, consequently, a simulation of length τ_{sim} has $60\omega_{\text{fast}}\tau_{\text{sim}}$ time steps. Because we want our simulations to be much longer than the period of the slowest chain mode, we expect the number of time steps to be at least $O(6000\omega_{\text{fast}})$. While the computational complexity of Eq. (A2) scales linearly with the number of time steps, Eq. (A1) has a quadratic scaling because every time step involves a summation over all previous time steps. Therefore, larger ω_{fast} leads to a much higher computational load. We have shown before [44] that $\Omega_{\text{fast}}/\Omega_{\text{slow}} = 10$ provides a sufficiently wide band while keeping the computational time reasonable. Hence, we set $\omega_{\text{fast}} = 10$ for this study.

As was mentioned above, Eq. (A1) is the computational bottleneck. Although one cannot circumvent the quadratic scaling with time steps, we reduce some of the load by precomputing the memory kernel, which is a parallelizable task, unlike the iterative solution of $\boldsymbol{\rho}$ and $\boldsymbol{\sigma}$. The precomputed kernel can also be reused as long as the chain parameters remain unchanged. For this precomputation, we define the time period for the simulation $\tau \in [0, \tau_{\text{sim}}]$ and partition this period into steps of size δ. Next, we fix the number of chain masses to be tracked during the simulation N_{ch} and calculate a matrix with elements $\Gamma_n(l\delta)$ for $0 \leqslant n \leqslant N_{\text{ch}} - 1, 1 \leqslant l \leqslant \tau_{\text{sim}}/\delta$ using the Gaussian quadrature method. Using double precision numbers, the total size of the matrix in the memory becomes $N_{\text{ch}}\tau_{\text{sim}}/\delta \times 8$ bytes, which, for our choice of δ and ω_{fast} with $N_{\text{ch}} = \tau_{\text{sim}} = 1000$, translates to $\approx$4.8 Gb. The precomputed kernel can now be used in various simulations as long as the simulation time and the number of chain masses do not exceed the precomputed values.

At each time step of the simulation, we calculate a matrix of pairwise forces $d\Phi(\rho_i, \sigma_j)/d\rho$. Summing the matrix along the rows gives total forces for each of the chain masses, while the negative sum along the columns results in the forces experienced by the mobile particles. Using the latter, the next column of the particle trajectory matrix $\overleftrightarrow{\sigma}$ is updated, following Eq. (A2).

To update the values of the chain trajectory matrix $\overleftrightarrow{\rho}$ using the most recently computed forces, it is possible to proceed in two ways. One involves first turning the precomputed kernel matrix into an array of Toeplitz matrices $[\overleftrightarrow{\Gamma}(\delta), \overleftrightarrow{\Gamma}(2\delta), \ldots, \overleftrightarrow{\Gamma}(\tau_{\text{sim}})]$. In the course of the simulation, we save all the forces acting on the chain segment at each time step. From this, we can compute the memory term by multiplying the past force vectors by the appropriate entries of the precomputed Toeplitz-$\overleftrightarrow{\Gamma}$ array and performing a summation. More specifically, $\overleftrightarrow{\Gamma}(0)$ is multiplied by the current force vector, $\overleftrightarrow{\Gamma}(\delta)$ by the force from the previous step, $\overleftrightarrow{\Gamma}(2\delta)$ by the force from two steps ago, and so on. In other words, $\overleftrightarrow{\Gamma}$'s with larger time arguments get multiplied by older forces. Although faithful to Eq. (A1), this approach is fairly slow because of the number of operations involved. A much more efficient approach involves propagating the effects of the interaction into the future instead of summing the past forces.

For this approach, we do not construct the Toeplitz matrices used in Eq. (A1) but instead arrange the precomputed values at the beginning of the simulation in the following manner:

$$\begin{pmatrix} \Gamma_{N_{\text{ch}}-1}(\delta) & \Gamma_{N_{\text{ch}}-1}(2\delta) & \ldots & \Gamma_{N_{\text{ch}}-1}(\tau_{\text{sim}}) \\ \vdots & \vdots & \ddots & \vdots \\ \Gamma_1(\delta) & \Gamma_1(2\delta) & \ldots & \Gamma_1(\tau_{\text{sim}}) \\ \Gamma_0(\delta) & \Gamma_0(2\delta) & \ldots & \Gamma_0(\tau_{\text{sim}}) \\ \Gamma_1(\delta) & \Gamma_1(2\delta) & \ldots & \Gamma_1(\tau_{\text{sim}}) \\ \vdots & \vdots & \ddots & \vdots \\ \Gamma_{N_{\text{ch}}-1}(\delta) & \Gamma_{N_{\text{ch}}-1}(2\delta) & \ldots & \Gamma_{N_{\text{ch}}-1}(\tau_{\text{sim}}) \end{pmatrix}. \tag{A3}$$

At every time step, after computing the forces experienced by every chain mass, we keep only the forces that are greater than a certain small value in magnitude (10^{-20} in our calculations) along with the corresponding chain mass indices. Next, for each mass in this set, we take a slice of N_{ch} rows from the matrix in Eq. (A3) so Γ_0 is on the row corresponding to the mass's index. We also keep only as many columns from this slice as there are remaining time steps in the simulation, dropping from the end. We multiply the matrix slice by $-2\pi\delta$ and the force, and add it to the future portion of $\overleftrightarrow{\rho}$. Adding the forcing this way is not only faster as it avoids matrix multiplication but it also makes saving the forces unnecessary, reducing the memory load.

[1] M. Razavy, *Classical and Quantum Dissipative Systems*, 2nd ed. (World Scientific Publishing, Singapore, 2017).

[2] G. S. Chen and X. Liu, *Friction Dynamics: Principles and Application* (Elsevier, 2016).

[3] R. Zwanzig, *Nonequilibrium Statistical Mechanics*, 1st ed. (Oxford University Press, New York, 2001).

[4] A. Altland and B. Simons, *Condensed Matter Field Theory*, 2nd ed. (Cambridge University Press, New York, 2010).

[5] R. K. Pathria and P. D. Beale, *Statistical Mechanics* (Elsevier, 2022).

[6] J. C. Bachman, S. Muy, A. Grimaud, H. H. Chang, N. Pour, S. F. Lux, O. Paschos, F. Maglia, S. Lupart, P. Lamp, L. Giordano, and Y. Shao-Horn, Inorganic solid-state electrolytes for lithium batteries: Mechanisms and properties governing ion conduction, Chem. Rev. **116**, 140 (2016).

[7] A. Manthiram, X. Yu, and S. Wang, Lithium battery chemistries enabled by solid-state electrolytes, Nat. Rev. Mats. **2**, 16103 (2017).

[8] T. Famprikis, P. Canepa, J. A. Dawson, M. S. Islam, and C. Masquelier, Fundamentals of inorganic solid-state electrolytes for batteries, Nat. Mater. **18**, 1278 (2019).

[9] I. I. E. Agency, Global EV Outlook 2020—Analysis—IWA (2020), IEA, Paris, https://www.iea.org/reports/global-ev-outlook-2020, License CC BY 4.0..

[10] Y. Yang, S. Bremner, C. Menictas, and M. Kay, Battery energy storage system size determination in renewable energy systems: A review, Renewable Sustainable Energy Rev. **91**, 109 (2018).

[11] Y. Wang, W. D. Richards, S. P. Ong, L. J. Miara, J. C. Kim, Y. Mo, and G. Ceder, Design principles for solid-state lithium superionic conductors, Nat. Mater. **14**, 1026 (2015).

[12] Y. Deng, C. Eames, J. N. Chotard, F. Laleíre, V. Seznec, S. Emge, O. Pecher, C. P. Grey, C. Masquelier, and M. S. Islam, Structural and mechanistic insights into fast lithium-ion conduction in $Li_4SiO_4 - Li_3PO_4$ solid electrolytes, J. Am. Chem. Soc. **137**, 9136 (2015).

[13] B. Kozinsky, S. A. Akhade, P. Hirel, A. Hashibon, C. Elsässer, P. Mehta, A. Logeat, and U. Eisele, Effects of Sublattice Symmetry and Frustration on Ionic Transport in Garnet Solid Electrolytes, Phys. Rev. Lett. **116**, 055901 (2016).

[14] N. J. D. Klerk and M. Wagemaker, Diffusion mechanism of the sodium-ion solid electrolyte Na_3Ps_4 and potential improvements of halogen doping, Chem. Mater. **28**, 3122 (2016).

[15] N. Adelstein and B. C. Wood, Role of dynamically frustrated bond disorder in a Li+ superionic solid electrolyte, Chem. Mater. **28**, 7218 (2016).

[16] X. He, Y. Zhu, and Y. Mo, Origin of fast ion diffusion in superionic conductors, Nat. Commun. **8**, 15893 (2017).

[17] T. Krauskopf, C. Pompe, M. A. Kraft, and W. G. Zeier, Influence of lattice dynamics on Na+ transport in the solid electrolyte $Na_3PS_{4-x}Se_x$, Chem. Mater. **29**, 8859 (2017).

[18] S. Muy, J. C. Bachman, L. Giordano, H. H. Chang, D. L. Abernathy, D. Bansal, O. Delaire, S. Hori, R. Kanno, F. Maglia, S. Lupart, P. Lamp, and Y. Shao-Horn, Tuning mobility and stability of lithium ion conductors based on lattice dynamics, Energy Environ. Sci. **11**, 850 (2018).

[19] Y. Deng, C. Eames, B. Fleutot, R. David, J. N. Chotard, E. Suard, C. Masquelier, and M. S. Islam, Enhancing the lithium ion conductivity in lithium superionic conductor (LISICON) solid electrolytes through a mixed polyanion effect, ACS Appl. Mater. Interfaces **9**, 7050 (2017).

[20] D. D. Stefano, A. Miglio, K. Robeyns, Y. Filinchuk, M. Lechartier, A. Senyshyn, H. Ishida, S. Spannenberger, D. Prutsch, S. Lunghammer, D. Rettenwander, M. Wilkening, B. Roling, Y. Kato, and G. Hautier, Superionic diffusion through frustrated energy landscape, Chem **5**, 2450 (2019).

[21] A. Carvalho, S. Negi, and A. H. C. Neto, Direct calculation of the ionic mobility in superionic conductors, Sci. Rep. **12**, 19930 (2022).

[22] A. Rodin, K. Noori, A. Carvalho, and A. H. Castro Neto, Microscopic theory of ionic motion in solids, Phys. Rev. B **105**, 224310 (2022).

[23] A. O. Caldeira and A. J. Leggett, Quantum tunnelling in a dissipative system, Ann. Phys. **149**, 374 (1983).

[24] B. L. Hu, J. P. Paz, and Y. Zhang, Quantum Brownian motion in a general environment: Exact master equation with nonlocal dissipation and colored noise, Phys. Rev. D **45**, 2843 (1992).

[25] A. Lampo, S. H. Lim, M. Ángel García-March, and M. Lewenstein, Bose polaron as an instance of quantum Brownian motion, Quantum **1**, 30 (2017).

[26] A. Petković, Microscopic theory of the friction force exerted on a quantum impurity in one-dimensional quantum liquids, Phys. Rev. B **101**, 104503 (2020).

[27] S.-I. Furusawa, H. Hayasi, Y. Ishibashi, A. Miyamoto, and T. Sasaki, Ionic conductivity of quasi-one-dimensional superionic conductor $KTiOPO_4$ (KTP) single crystal, J. Phys. Soc. Jpn. **62**, 183 (1993).

[28] S.-I. Furusawa, H. Sugiyama, F. Itoh, A. Miyamoto, and T. Sasaki, Ionic conductivity of quasi-one-dimensional ionic conductor $KTiOPO_4$ (KTP) single crystal at high pressure, J. Phys. Soc. Jpn. **69**, 2087 (2000).

[29] M. Månsson, I. Umegaki, H. Nozaki, Y. Higuchi, I. Kawasaki, I. Watanabe, H. Sakurai, and J. Sugiyama, Na-ion dynamics in Quasi-1D compound NaV_2O_4, J. Phys. Conf. Ser. **551**, 012035 (2014).

[30] K. Volgmann, V. Epp, J. Langer, B. Stanje, J. Heine, S. Nakhal, M. Lerch, M. Wilkening, and P. Heitjans, Solid-state NMR to study translational Li ion dynamics in solids with low-dimensional diffusion pathways, Z. Phys. Chem. **231**, 1215 (2017).

[31] K.-H. Cho and P. K. Jain, Superionic conduction in one-dimensional nanostructures, ACS Nano **16**, 12445 (2022).

[32] M. C. Lim and Z. W. Zhong, Dynamical behavior of copper atoms in a carbon nanotube channel, Carbon **49**, 996 (2011).

[33] R. Senga, H.-P. Komsa, Z. Liu, K. Hirose-Takai, A. V. Krasheninnikov, and K. Suenaga, Atomic structure and dynamic behaviour of truly one-dimensional ionic chains inside carbon nanotubes, Nat. Mater. **13**, 1050 (2014).

[34] R. H. Tunuguntla, F. I. Allen, K. Kim, A. Belliveau, and A. Noy, Ultrafast proton transport in sub-1-nm diameter carbon nanotube porins, Nat. Nanotechnol. **11**, 639 (2016).

[35] A. W. Hauser, A. O. Mitrushchenkov, and M. P. D. Lara-Castells, Quantum nuclear motion of helium and molecular nitrogen clusters in carbon nanotubes, J. Phys. Chem. C **121**, 3807 (2017).

[36] A. N. Khlobystov, D. A. Britz, and G. A. D. Briggs, Molecules in carbon nanotubes, Acc. Chem. Res. **38**, 901 (2005).

[37] S. Chen, Y. Cheng, G. Zhang, and Y. W. Zhang, Spontaneous directional motion of water molecules in single-walled carbon nanotubes with a stiffness gradient, Nanoscale Advances **1**, 1175 (2019).

[38] A. N. Khlobystov, K. Porfyrakis, M. Kanai, D. A. Britz, A. Ardavan, H. Shinohara, T. J. S. Dennis, and G. A. D. Briggs, Molecular motion of endohedral fullerenes in single-walled carbon nanotubes, Angew. Chem. Int. Ed. **43**, 1386 (2004).

[39] M. D. C. Gimenez-Lopez, A. Chuvilin, U. Kaiser, and A. N. Khlobystov, Functionalised endohedral fullerenes in single-walled carbon nanotubes, Chem. Commun. **47**, 2116 (2011).

[40] https://github.com/rodin-physics/1d-chain-thermalization.

[41] J. Bezanson, A. Edelman, S. Karpinski, and V. B. Shah, Julia: A fresh approach to numerical computing, Soc. Ind. Appl. Math. **59**, 65 (2017).

[42] S. Danisch and J. Krumbiegel, Makie.jl: Flexible high-performance data visualization for Julia, J. Open Source Software **6**, 3349 (2021).

[43] B. Wong, Color blindness, Nat. Methods **8**, 441 (2011).

[44] A. Rodin, B. A. Olsen, M. Choi, and A. Tan, Microscopic theory of thermalization in one dimension with nonlinear bath coupling, Phys. Rev. Res. **4**, 033057 (2022).

[45] C. Franchini, M. Reticcioli, M. Setvin, and U. Diebold, Polarons in materials, Nat. Rev. Mater. **6**, 560 (2021).

[46] K. Parlinski, *Lattice Dynamics: Vibrational Modes* (Elsevier, 2005).